

Nonlinear vibration response of a complex aeroengine under the rubbing fault

Jingze Liu

Southeast University

Qingguo Fei (✉ qgfei@seu.edu.cn)

School of Mechanical Engineering, Southeast University

Shaoqing Wu

Southeast University

Zhenhuan Tang

China Aviation Power Plant Research Institute

Dahai Zhang

Southeast University

Research Article

Keywords: whole aeroengine model, nonlinear vibration analysis, rolling bearing, squeeze film damper, rubbing, bifurcation

Posted Date: June 21st, 2021

DOI: <https://doi.org/10.21203/rs.3.rs-242862/v1>

License:   This work is licensed under a Creative Commons Attribution 4.0 International License.

[Read Full License](#)

Version of Record: A version of this preprint was published at Nonlinear Dynamics on October 12th, 2021. See the published version at <https://doi.org/10.1007/s11071-021-06717-4>.

Nonlinear vibration response of a complex aeroengine under the rubbing fault

Jingze Liu^{1,2}, Qingguo Fei^{1,2,*}, Shaoqing Wu^{1,3}, Zhenhuan Tang⁴, Dahai Zhang^{1,2}

¹*Jiangsu Engineering Research Center of Aerospace Machinery, Nanjing 211189, China*

²*School of Mechanical Engineering, Southeast University, Nanjing 211189, China*

³*Department of Engineering Mechanics, Southeast University, Nanjing 211189, China*

⁴*China Aviation Power Plant Research Institute, Zhuzhou 412002, China*

Abstract: Rolling bearing and squeeze film damper will introduce structural nonlinearity into the dynamic model of aeroengine. Rubbing will occur due to the clearance reduction design of the engine. The coupling of structural nonlinearity and fault nonlinearity will make the engine present rich vibration responses. This paper aims to analyze the nonlinear vibration behavior of the whole aeroengine including rolling bearing and squeeze film damper under rubbing fault. Firstly, the dynamic model of a turboshaft engine with nonlinear support and rubbing fault is established; The rolling bearing force, the oil film force and the rubbing force are introduced into a dual-rotor-casing model with six support points. Secondly, the linear part of the model is verified by the dynamic characteristics of the three-dimensional finite element model. Finally, the varying compliance vibration, the damping effect and the bifurcation mechanism are analyzed in detail in which the bearing clearance, speed ratio and rubbing stiffness are considered. Results show that the rubbing fault in the nonlinear support case will excite more significant varying compliance vibration in the low-speed region and expand the rotating speed range of the chaotic region in the high-speed region compared with that in the linear support case.

Keywords: *whole aeroengine model; nonlinear vibration analysis; rolling bearing; squeeze film damper; rubbing; bifurcation*

1 Introduction

The rotor-bearing-casing system is the core structure of a whole aeroengine including multi-nonlinearities. To reduce the vibration level during operation, the supporting structures are generally composed of rolling bearing and squeeze film damper (SFD). The complex relationships among these supports lead to the strong nonlinearity of the whole system. As the clearance between blade and casing becomes smaller and smaller for higher efficiency, the rub impact of blade casing will be easily caused by the nonlinear supports, which will exhibit more complex nonlinearity [1]. These nonlinear factors will have a very distinct influence on the motion form and stability of the aeroengine. According to the actual need in practice, accurate prediction of the nonlinear dynamic response is the key issue to solving structural design problems. Therefore, it's necessary to investigate the nonlinear dynamic response of the rotor-bearing-casing system considering the multi-nonlinearities including nonlinear bearing force, nonlinear oil film force and nonlinear rubbing force.

A three-dimensional (3D) finite element model is the model that can best reflect the real structure of an aeroengine. These models created by a fine mesh are widely used for dynamic characteristics [2,4], stochastic response [3] and vibration energy transmission [5]. Although the finite element model with 3D solid elements is adapted to represent the structural characteristics of aeroengine, the nonlinear factors of rolling bearing, SFD and rubbing in these 3D whole aeroengine models have rarely been considered. The reason is that when these nonlinearities are considered in these finite element models, the computational cost for the dynamic characteristic and response analysis will be extremely large, which limits the application of this kind of modeling technique.

For that reason, many scholars have carried out abundant research considering the nonlinearities of bearing and oil film using the beam models. Because the beam models are easier to be established and improve computational efficiency. In some models, only the nonlinear bearing forces were considered [6-11]. In other models, only nonlinear oil film forces were considered [12-

* Corresponding author.

E-mail address: qgfei@seu.edu.cn (Q. Fei)

19]. However, the supporting structure of a real aeroengine is a combination of SFD and rolling bearing. Due to the internal interaction of the composite supports, complex nonlinear supporting forces are generated, and the system exhibits abundant nonlinear phenomena. Thus, more and more scholars consider both nonlinear forces simultaneously in system modeling. The non-synchronous responses [20], the nonlinear dynamic response under bearing inner race defect [21] and the stability at different locations [22] were studied for single rotor systems respectively. More abundant nonlinear dynamic response research and experimental verification were carried out for a double-rotor system with dual-frequency excitation [23]. However, the nonlinear dynamic characteristics of the whole aeroengine can't be truly reflected only through the research of the rotor system. The flexibility of the casing is another important factor that must be considered. Furthermore, based on the combined supporting structure, some researchers studied the nonlinear dynamics of the whole aeroengine model including the casing [24-30], to more precisely describe the nonlinear dynamic behavior of the structure.

In addition to the nonlinearity of support, scholars were also constantly studying the complex vibration problems caused by fault nonlinearity. The nonlinear vibrations of the aeroengine structure may lead to various kinds of vibration faults, e.g. the blade casing rub [31]. More serious nonlinearity will be caused by the blade casing rub, which has been studied by many researchers. In a considerable part of rubbing studies [32-42], nonlinear bearings were often linearized as linear spring for the convenience of model simplification. However, in the real situation, the supporting structure of an aeroengine is composed of rolling bearings and SFDs, and there is a complex displacement relationship between the supporting parts. Anisotropy is the inherent characteristic of the support structures [23]. The expression of linear spring and damping is not capable of describing the complex nonlinear displacement relationship in the supporting structure. Besides, the complex nonlinear vibration caused by the supporting structure is also the source of many faults of the aero-engine, such as rubbing. So, the over-simplified linear supports cannot accurately predict the response of the whole structure. The supporting structure must be considered as nonlinear in the analysis of the whole aeroengine with rub fault.

As the research moves along, the nonlinearity of the support was gradually considered in the study of rubbing. The vibration under the coupling effect of nonlinear support and rubbing was revealed by numerical and experimental methods. In the early years, many scholars studied the nonlinear dynamics of simple single rotor systems by combining the nonlinear oil film force and rubbing force [43-48]. Although the bifurcation and chaos mechanisms caused by nonlinear support and rubbing can be revealed, these models are unable to include the dual-frequency excitation in more complex double-rotor systems. Later, the mechanism of nonlinear support and rubbing under dual-frequency excitation attracted more attention. Wang et al. [49] and Jin et al. [50] adopted a more complex double-rotor-bearing system to conduct nonlinear rubbing dynamics research. More complex frequency combinations were observed, which explained the complexity of the dynamic behavior of the dual-rotor system. In addition to the dual-rotor system, the casing is another important structure in a complete aeroengine. The path of force transmission between the rotor and the aircraft is rotor-support-bearing house-strut-casing-mounting joint-aircraft. Therefore, it is of engineering significance to study the rubbing vibration of the whole machine in a complete rotor-bearing-casing system. In recent years, in consideration of only the nonlinearity of the rolling bearing, the rubbing mechanism of a rotor-bearing-casing system was revealed by Chen [51,52] and Yang et al. [53]. Although rolling bearings or SFDs are considered in these rub studies, the actual supporting structure is a combination of them. The nonlinear bearing forces and the nonlinear oil film forces coexist in an aeroengine system. Under the combined action of the dynamic characteristics of oil film and the time-varying contact of the rolling body, the rubbing fault of a whole aeroengine needs to be more comprehensively studied.

The above studies on rubbing faults can be divided into two categories according to whether the casing was considered. Emphasis was put on the single rotor or dual-rotor without casing in references [32-36,38-40,42-46,48-50]. Considering the flexibility of the casing, researchers paid attention to the nonlinearity of the rotor-bearing-casing [37,41,51-53]. The nonlinear bearing force and the nonlinear oil film force were not considered simultaneously in these rub researches. The bearing force, nonlinear oil film force and nonlinear rubbing force are only considered simultaneously in a rotor system [54] and a rotor-ball bearing-stator coupling system with a single rotor [24]. Most of the real aeroengine structures contain dual-rotor structures, and the rub impact mechanism under double-frequency excitation is more complex [17]. Overall, the mechanism of the nonlinear vibration of the whole dual-rotor aeroengine system under multi-nonlinearities, which including the nonlinear Hertz contact force from rolling bearing, the nonlinear oil film force from SFD and the nonlinear rubbing force, etc., should be further studied to make the analysis closer to the real status of a whole aeroengine, that is the inspiration of this study.

This research work aims to establish a dual-rotor-rolling bearing-SFD-casing system for studying the mechanism of the nonlinear vibration of whole dual-rotor aeroengine system under multi-nonlinearities including the nonlinear Hertz contact force from rolling bearing, the nonlinear oil film force from SFD and the nonlinear rubbing force. The following paper is organized as follows. In Section 2, a dual-rotor whole engine model is established according to a real turboshaft engine. The nonlinear rolling bearing force, the nonlinear film force of the SFD and blade-casing rub are all considered. In Section 3, the dynamic characteristics of the linear part of the engine's model are verified by that of the corresponding complete 3D finite element model. In the fourth section, the VC vibration of the rolling bearing, the damping effect of the extruded oil film damper, and the bifurcation phenomenon caused by rubbing under linear/nonlinear supports are all studied. An in-depth parametric analysis involving bearing clearance, oil film thickness, rotating speed ratio, and rubbing stiffness was performed.

2 Methodology

2.1 Simplification and finite element modeling of the aeroengine

A dual-rotor turboshaft aero-engine is shown in Fig. 1. The gas generator rotor is a high-pressure rotor, which is supported by two bearings (Bearing3, Bearing4). The power turbine rotor is a low-pressure rotor, which is supported by four bearings (Bearing1, Bearing2, Bearing5, Bearing6). The front housing is shared by bearing1 to bearing3, while the back housing is shared by bearing4 to bearing6. The load is transferred between the housing and casing through an integrated strut. Oil film exists between the outer ring of each bearing and the housing. The existence of the SFD can reduce the vibration of the rotor.

The real aeroengine structure is very complex as shown in Fig. 1. The complete 3D finite element model based on the real structure is usually not suitable for nonlinear vibration analysis because of its high computational cost. Therefore, a simplified finite element model which can reflect the dynamic characteristics of the structure is often adopted in this case [25]. The principles of simplification are as follows:

- (1) The rotating shafts are considered as beam elements which include shear deformations, gyroscopic moments and inertia.
- (2) The disks are assumed as mass elements without considering deformation.
- (3) The casing and housing are considered as beam elements without gyroscopic moments.
- (4) The connections between casing and foundation, casing and housing, as well as the squirrel cages are considered as linear springs.
- (5) The forces between the bearing outer ring and the rotor are considered as nonlinear bearing forces.
- (6) The forces between the bearing outer ring and the bearing housing are considered as nonlinear oil film forces.

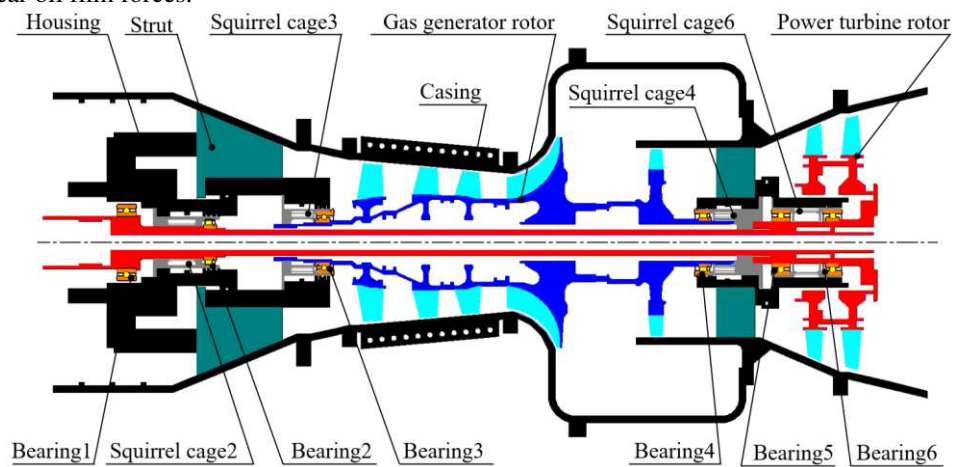


Fig. 1 Sketch of a dual-rotor turboshaft aeroengine with six supports

According to the simplification principles and the structure of the real turboshaft engine, a simplified finite element model as shown in Fig. 2 can be established. The finite element model consists of 30 elements and 41 nodes. The casing, rotor and housing are all modeled by beam elements. The outer ring of the bearing and blade disk is modeled by discrete mass. Linear springs

and dampers are used to model mounting joints and struts. Both the nonlinear bearing force and oil film force are adopted to model different kinds of contact load between rotor and housing. The rubbing force model is introduced at the rubbing point. All the components are coupled by linear springs and nonlinear forces, and a nonlinear dynamic model of the whole aeroengine is formulated.

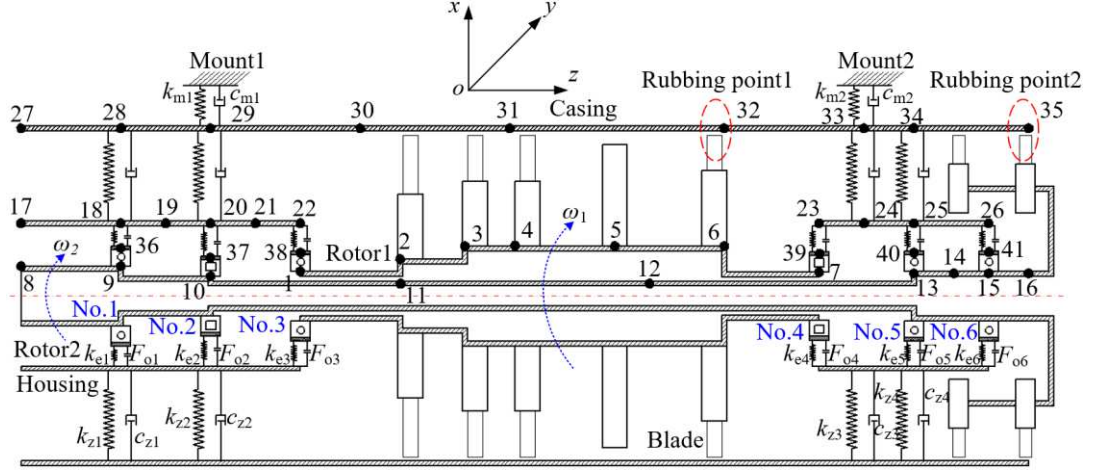


Fig. 2 Finite element model of the whole aeroengine

2.2 Rolling bearing force model

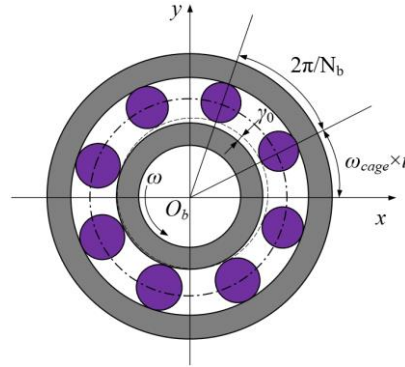


Fig. 3 Cross-section of rolling bearing

The cross-section of a typical rolling bearing is shown in Fig. 3. The rolling bearing is composed of inner ring, outer ring, rolling element and cage. According to the Hertz contact theory, contact deformation between the rolling element and raceway will produce a nonlinear restoring force. For ball bearing, the bearing force can be expressed as [55],

$$F_{bx} = \sum_{j=1}^{N_b} C_b (x \cos \beta_j + y \sin \beta_j - \gamma_0)^{3/2} H(x \cos \beta_j + y \sin \beta_j - \gamma_0) \cos \beta_j \quad (1)$$

$$F_{by} = \sum_{j=1}^{N_b} C_b (x \cos \beta_j + y \sin \beta_j - \gamma_0)^{3/2} H(x \cos \beta_j + y \sin \beta_j - \gamma_0) \sin \beta_j$$

For roller bearing, the bearing force can be expressed as [56],

$$F_{bx} = \sum_{j=1}^{N_b} C_b (x \cos \beta_j + y \sin \beta_j - \gamma_0)^{10/9} H(x \cos \beta_j + y \sin \beta_j - \gamma_0) \cos \beta_j \quad (2)$$

$$F_{by} = \sum_{j=1}^{N_b} C_b (x \cos \beta_j + y \sin \beta_j - \gamma_0)^{10/9} H(x \cos \beta_j + y \sin \beta_j - \gamma_0) \sin \beta_j$$

where N_b is the number of rolling elements, C_b is the Hertz contact stiffness, x and y represent the relative displacements between the rotor and outer ring in x - and y - directions respectively,

$$x = x_{rotor} - x_{outring} \quad (3)$$

$$y = y_{rotor} - y_{outring}$$

$H(\cdot)$ is the Heaviside function, γ_0 is the radial clearance of bearing, β_j is the angle of j^{th} rolling element, and

$$\beta_j = \omega_{cage} \times t + 2\pi / N_b (j-1), j=1,2,\dots,N_b \quad (4)$$

$$\omega_{cage} = \frac{\omega R_i}{R_0 + R_i} \quad (5)$$

ω_{cage} is the rotating speed of the cage, ω is the rotating speed of the rotor, R_i is the radius of the inner ring, and R_0 is the radius of the outer ring.

2.3 Oil film force model

The structure of SFD is shown in Fig. 4. A certain clearance is reserved between the outer ring of the bearing and the housing. The rotation of the outer ring of the bearing is restricted by the squirrel cage which is elastic support for the rotor. Lubricating oil fills the gap between the outer ring of the bearing and the housing. The viscous damping of the lubricating oil plays an important role in reducing the vibration of the rotor. According to the assumption of short bearing, the nonlinear oil film force in x and y directions is [57]

$$\begin{aligned} F_{oilx} &= -\frac{\mu RL^3}{C^2 \sqrt{X_i^2 + Y_i^2}} [X_i(I_1 \varepsilon' + I_2 \varepsilon \phi') - Y_i(I_2 \varepsilon' + I_3 \varepsilon \phi')] \\ F_{oily} &= -\frac{\mu RL^3}{C^2 \sqrt{X_i^2 + Y_i^2}} [Y_i(I_1 \varepsilon' + I_2 \varepsilon \phi') + X_i(I_2 \varepsilon' + I_3 \varepsilon \phi')] \end{aligned} \quad (6)$$

where μ is the viscosity of lubricating oil, R is the radius of damper, L is the length of damper, C is the clearance of SFD, $X_i = x_i/C$, $Y_i = y_i/C$, x_i and y_i are the relative displacements of the outer ring of the bearing and the housing in x- and y- directions respectively.

$$\begin{aligned} x_i &= x_{outering} - x_{housing} \\ y_i &= y_{outering} - y_{housing} \end{aligned} \quad (7)$$

ε is eccentricity,

$$\begin{aligned} \varepsilon &= \sqrt{X_i^2 + Y_i^2} \\ \varepsilon' &= \frac{x_i \dot{x}_i + y_i \dot{y}_i}{C \sqrt{x_i^2 + y_i^2}} \end{aligned} \quad (8)$$

ϕ is the angle of journal precession and ϕ' is its first derivative, and

$$\begin{aligned} \phi &= \arctan\left(\frac{y_i}{x_i}\right) \\ \phi' &= \frac{x_i \dot{y}_i - y_i \dot{x}_i}{x_i^2 + y_i^2} \end{aligned} \quad (9)$$

I_1 , I_2 and I_3 are the Sommerfeld integrals, θ_1 is the starting point of the oil film positive pressure zone,

$$\begin{aligned} I_1 &= \int_{\theta_1}^{\theta_1 + \pi} \frac{\cos^2 \theta}{(1 + \varepsilon \cos \theta)^3} d\theta \\ I_2 &= \int_{\theta_1}^{\theta_1 + \pi} \frac{\sin \theta \cos \theta}{(1 + \varepsilon \cos \theta)^3} d\theta \\ I_3 &= \int_{\theta_1}^{\theta_1 + \pi} \frac{\sin^2 \theta}{(1 + \varepsilon \cos \theta)^3} d\theta \\ \theta_1 &= \arctan\left(-\frac{\varepsilon'}{\varepsilon \phi'}\right) \end{aligned} \quad (10)$$

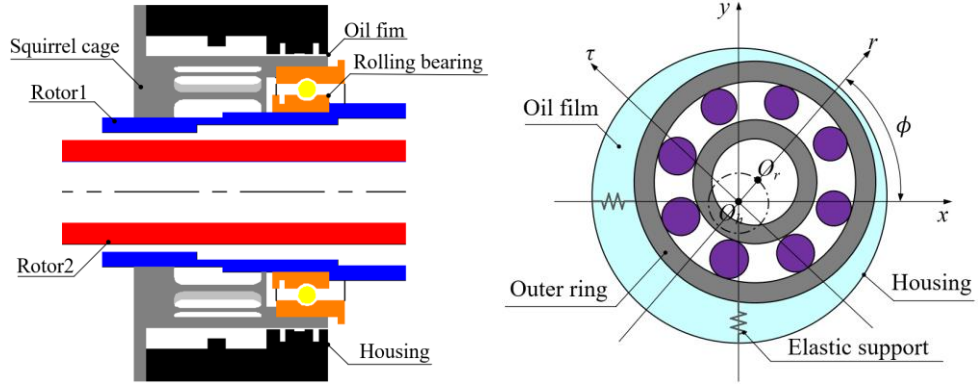


Fig. 4 Sketch of SFD

2.4 Rubbing force model

A typical blade casing rubbing model is shown in Fig. 5. By setting local deformation at one position of the casing, the single point rubbing of the casing is realized. Assuming that the rotating speed is ω , the number of blades on the disk is N , the initial clearance between the rotor and stator is δ , k_c is the stiffness of casing, A is the deformation of the casing at angle θ . The rubbing region is in the angle range within $\pm\beta$. The radial displacement of the blade and casing can be expressed as

$$\begin{aligned} d_{bi} &= x_{blade} \cos(\theta_{bi}) + y_{blade} \sin(\theta_{bi}) \\ d_{ci} &= x_{casing} \cos(\theta_{bi}) + y_{casing} \sin(\theta_{bi}) \end{aligned} \quad (11)$$

where θ_{bi} is the angle between the i^{th} blade and x-axis at time t ,

$$\theta_{bi} = 2\pi i / N + \omega t \quad (12)$$

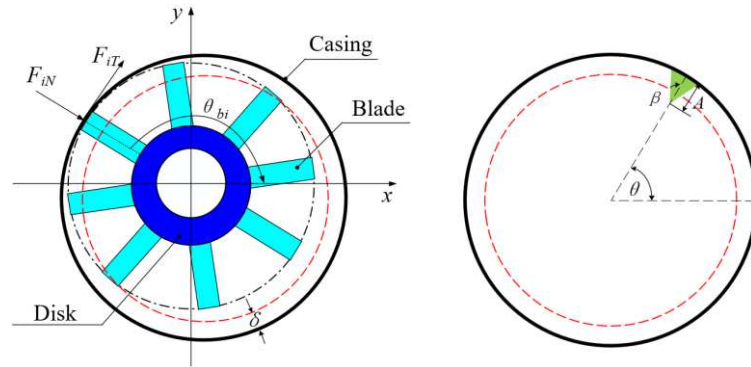


Fig. 5 Blade casing rubbing model

The normal rubbing force can be expressed as

$$\begin{aligned} F_{iNx} &= -F_{iN} \cos(\theta_{bi}) \\ F_{iNy} &= -F_{iN} \sin(\theta_{bi}) \end{aligned} \quad (13)$$

where

$$F_{iN} = \frac{1}{2} k_c \{ |d_{bi} - d_{ci} - \delta(\theta_{bi})| + [d_{bi} - d_{ci} - \delta(\theta_{bi})] \} \quad (14)$$

$$\delta(\theta_{bi}) = \begin{cases} \delta, & |\theta_{bi} - \theta| > \beta \\ \delta - A[0.5 + 0.5 \cos \frac{\pi(\theta_{bi} - \theta)}{\beta}], & |\theta_{bi} - \theta| \leq \beta \end{cases} \quad (15)$$

The tangential rubbing force can be expressed as

$$\begin{aligned} F_{iT_x} &= F_{iT} \sin(\theta_{bi}) \\ F_{iT_y} &= -F_{iT} \cos(\theta_{bi}) \end{aligned} \quad (16)$$

where

$$F_{iT} = fF_{iN} \quad (17)$$

f is the coefficient of friction.

Consequently, at time t , the rubbing force acting on the rotor can be expressed as the combined rubbing force of N blades [58,59].

$$\begin{aligned} F_{rubx} &= \sum_{i=1}^N (F_{iNx} + F_{iT_x}) \\ F_{rubby} &= \sum_{i=1}^N (F_{iNy} + F_{iT_y}) \end{aligned} \quad (18)$$

2.5 Governing equation of the coupling system

Rotor1, rotor2, housing and casing are all modeled by beam elements that have 4 degrees-of-freedom (DOFS) for each node. The outer ring of the bearing is modeled by mass points containing 2 DOFS.

The governing equation of rotor1 can be expressed as

$$\mathbf{M}_{r1} \ddot{\mathbf{u}}_{r1} + (\mathbf{C}_{r1} - \omega_1 \mathbf{G}_{r1}) \dot{\mathbf{u}}_{r1} + \mathbf{K}_{r1} \mathbf{u}_{r1} = \mathbf{F}_{r1} \quad (19)$$

$$\mathbf{F}_{r1} = [\cdots, -\mathbf{F}_{b1}, \cdots, \mathbf{F}_{u1}, \cdots, -\mathbf{F}_{rub1}, \cdots, \mathbf{F}_{gr1}] \quad (20)$$

where, $\mathbf{u}_{r1i} = [x_{r1i}, y_{r1i}, \theta_{xr1i}, \theta_{yr1i}]^T$ is the displacement for the i^{th} node of rotor1, ω_1 is the rotating speed of rotor1. \mathbf{M}_{r1} , \mathbf{C}_{r1} , \mathbf{G}_{r1} and \mathbf{K}_{r1} are the mass matrix, damping matrix, gyroscopic matrix and stiffness matrix respectively. Rayleigh damping is assumed. The generalized external force \mathbf{F}_{r1} is composed of the bearing force \mathbf{F}_{b1} , the unbalanced force \mathbf{F}_{u1} , the rubbing force \mathbf{F}_{rub1} and the force of gravity \mathbf{F}_{gr1} . The unbalanced force on the i^{th} node of rotor1 is $\mathbf{F}_{u1i} = [m_{r1i}e_i\omega_1^2 \cos\omega_1 t, m_{r1i}e_i\omega_1^2 \sin\omega_1 t]^T$.

The governing equation of rotor2 can be expressed as

$$\mathbf{M}_{r2} \ddot{\mathbf{u}}_{r2} + (\mathbf{C}_{r2} - \omega_2 \mathbf{G}_{r2}) \dot{\mathbf{u}}_{r2} + \mathbf{K}_{r2} \mathbf{u}_{r2} = \mathbf{F}_{r2} \quad (21)$$

$$\mathbf{F}_{r2} = [\cdots, -\mathbf{F}_{b2}, \cdots, \mathbf{F}_{u2}, \cdots, -\mathbf{F}_{rub2}, \cdots, \mathbf{F}_{gr2}] \quad (22)$$

where, $\mathbf{u}_{r2i} = [x_{r2i}, y_{r2i}, \theta_{xr2i}, \theta_{yr2i}]^T$ is the displacement for the i^{th} node of rotor2, ω_2 is the rotating speed of rotor2. \mathbf{M}_{r2} , \mathbf{C}_{r2} , \mathbf{G}_{r2} and \mathbf{K}_{r2} are the mass matrix, damping matrix, gyroscopic matrix and stiffness matrix respectively. Rayleigh damping is applied. The generalized external force \mathbf{F}_{r2} is composed of the bearing force \mathbf{F}_{b2} , the unbalanced force \mathbf{F}_{u2} , the rubbing force \mathbf{F}_{rub2} and the force of gravity \mathbf{F}_{gr2} . The unbalanced force on the i^{th} node of rotor2 is $\mathbf{F}_{u2i} = [m_{r2i}e_i\omega_2^2 \cos\omega_2 t, m_{r2i}e_i\omega_2^2 \sin\omega_2 t]^T$.

The governing equation of casing can be expressed as

$$\mathbf{M}_c \ddot{\mathbf{u}}_c + \mathbf{C}_c \dot{\mathbf{u}}_c + \mathbf{K}_c \mathbf{u}_c = \mathbf{F}_c \quad (23)$$

$$\mathbf{F}_c = [\cdots, \mathbf{F}_{ch}, \cdots, \mathbf{F}_{rub}, \cdots, \mathbf{F}_{gc}] \quad (24)$$

where, the displacement for the i^{th} node of the casing is $\mathbf{u}_{ci} = [x_{ci}, y_{ci}, \theta_{xci}, \theta_{yci}]^T$, \mathbf{M}_c , \mathbf{C}_c and \mathbf{K}_c are the mass matrix, damping matrix and stiffness matrix respectively. Rayleigh damping is applied. The generalized external force \mathbf{F}_c is composed of the elastic force \mathbf{F}_{ch} between the housing and the casing, the rubbing force \mathbf{F}_{rub} and the force of gravity \mathbf{F}_{gc} , $\mathbf{F}_{ch} = \mathbf{K}_s \mathbf{u}_c - \mathbf{K}_s \mathbf{u}_h$.

The governing equation of housing can be expressed as

$$\mathbf{M}_h \ddot{\mathbf{u}}_h + \mathbf{C}_h \dot{\mathbf{u}}_h + \mathbf{K}_h \mathbf{u}_h = \mathbf{F}_h \quad (25)$$

$$\mathbf{F}_h = [\cdots, -\mathbf{F}_{ch}, \cdots, -\mathbf{F}_{ho}, \cdots, \mathbf{F}_{oil}, \cdots, \mathbf{F}_{gh}] \quad (26)$$

(kg/m ³)	8240	8240	8240	8240	8240	8240	8240	8240
Mass of disk	m_2	m_3	m_4	m_5	m_6	m_{14}	m_{16}	
(kg)	1.008	0.393	0.177	3.253	3.395	2.859	4.345	
Diametric inertial moment	J_{dd2}	J_{dd3}	J_{dd4}	J_{dd5}	J_{dd6}	J_{dd14}	J_{dd16}	
(10 ⁻⁶ kg·m ²)	1.05	0.438	0.145	7.438	5.763	9.15	13.95	
Polar inertial moment	J_{pd2}	J_{pd3}	J_{pd4}	J_{pd5}	J_{pd6}	J_{pd14}	J_{pd16}	
(10 ⁻⁶ kg·m ²)	1.945	0.856	0.289	14.21	11.13	17.49	25.13	
Poisson's ratio	0.3							

As shown in Fig. 2, the connections in the whole aeroengine model contain both linear and nonlinear parts. The mount, the strut and the squirrel cage are linear parts, while the rolling bearing and the SFDs are nonlinear parts. To verify the accuracy of the linear part of the model, a comparative study on the dynamic characteristics of the complete 3D finite element model will be conducted in this Section. The structural dimensions and material parameters for rotors and stators are respectively shown in Table 1 and Table 2. A 3D finite element model of a whole aeroengine as shown in Fig. 6 is established in the commercial finite element software. All the nonlinearities in SFDs and rolling bearings are ignored and these connections are replaced by linear springs. According to the supporting form in Fig. 1, the first fulcrum and fifth fulcrum are assumed as rigid supports with stiffness coefficients equal to 10×10^7 N/m. The other four fulcrum points are regarded as elastic supports with stiffness coefficients equal to 2.5×10^7 N/m. The results of the first three vibration modes calculated from the proposed model are compared with those obtained by the 3D finite element model in Table 3 and Fig. 7. The errors in the modal frequencies are 5.2%, 4.1% and 3.3%, respectively. The accuracy of the linear part of the model is verified by the coincidence of mode shape and frequency. Based on the verified linear part of the model, the nonlinear behavior of the whole aeroengine will be carried out by adding the nonlinear bearing force, oil film force and rubbing force on the verified linear part of the model.

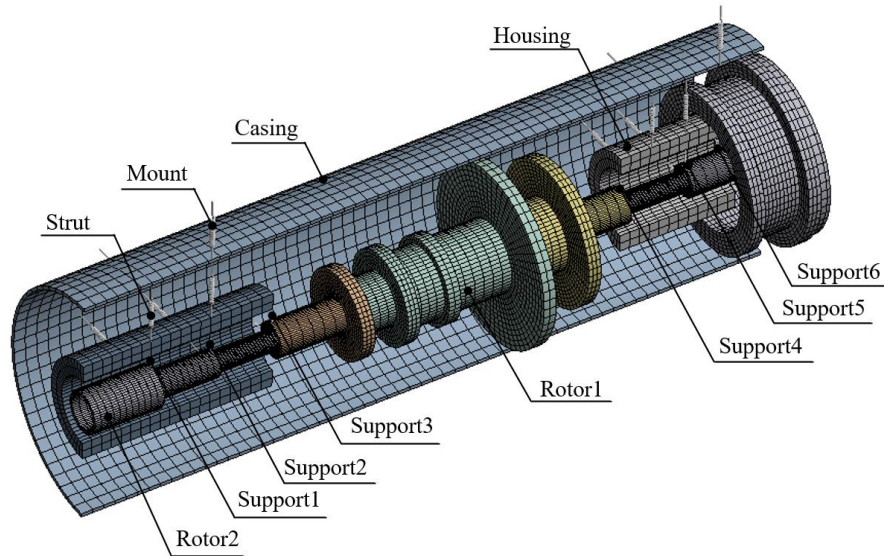


Fig. 6 Finite element model with 3D solid elements for the whole aeroengine

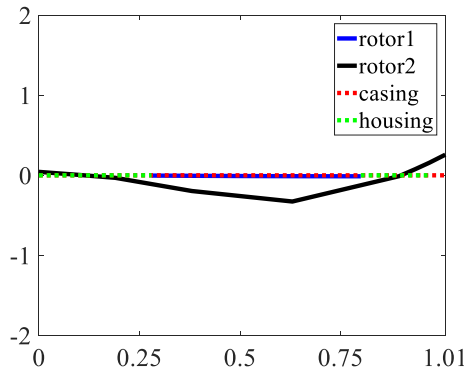
Table 2 The structural dimensions and material parameters for stators

Parameter	The value between the i^{th} node and the j^{th} node							
Length of housing (m)	L_{1718}	L_{1819}	L_{1920}	L_{2021}	L_{2122}	L_{2324}	L_{2425}	L_{2526}
	0.1	0.045	0.045	0.045	0.045	0.045	0.05	0.075
Length of casing (m)	L_{2728}	L_{2829}	L_{2930}	L_{3031}	L_{3132}	L_{3233}	L_{3334}	L_{3435}
	0.1	0.09	0.15	0.15	0.215	0.14	0.05	0.115
Outer diameter of housing (m)	D_{1718}	D_{1819}	D_{1920}	D_{2021}	D_{2122}	D_{2324}	D_{2425}	D_{2526}
	0.15	0.15	0.15	0.15	0.15	0.15	0.15	0.15

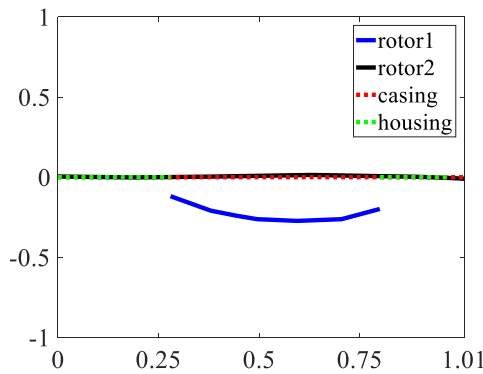
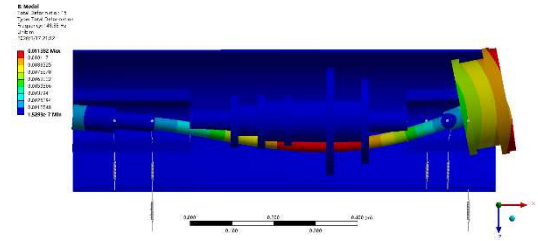
Outer diameter of casing (m)	D_{2728}	D_{2829}	D_{2930}	D_{3031}	D_{3132}	D_{3233}	D_{3334}	D_{3435}
	0.338	0.338	0.338	0.338	0.338	0.338	0.338	0.338
Inner diameter of housing (m)	d_{1718}	d_{1819}	d_{1920}	d_{2021}	d_{2122}	d_{2324}	d_{2425}	d_{2526}
	0.1	0.1	0.1	0.1	0.1	0.1	0.1	0.1
Inner diameter of casing (m)	d_{2728}	d_{2829}	d_{2930}	d_{3031}	d_{3132}	d_{3233}	d_{3334}	d_{3435}
	0.33	0.33	0.33	0.33	0.33	0.33	0.33	0.33
Elastic modulus of housing (GPa)	E_{1718}	E_{1819}	E_{1920}	E_{2021}	E_{2122}	E_{2324}	E_{2425}	E_{2526}
	210	210	210	210	210	210	210	210
Elastic modulus of casing (GPa)	E_{2728}	E_{2829}	E_{2930}	E_{3031}	E_{3132}	E_{3233}	E_{3334}	E_{3435}
	210	210	210	210	210	210	210	210
Density of housing (kg/m^3)	ρ_{1718}	ρ_{1819}	ρ_{1920}	ρ_{2021}	ρ_{2122}	ρ_{2324}	ρ_{2425}	ρ_{2526}
	7850	7850	7850	7850	7850	7850	7850	7850
Density of casing (kg/m^3)	ρ_{2728}	ρ_{2829}	ρ_{2930}	ρ_{3031}	ρ_{3132}	ρ_{3233}	ρ_{3334}	ρ_{3435}
	7850	7850	7850	7850	7850	7850	7850	7850
Poisson's ratio	0.3							

Table 3 Comparisons of first three order frequencies between the proposed model and the 3D model (Hz)

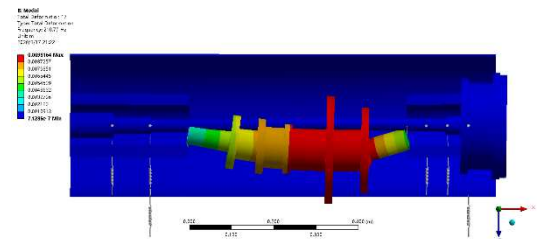
Mode order	Proposed model	3D model	Errors (%)
1	140.73	148.38	5.2
2	210.79	219.53	4.1
3	270.12	261.47	3.3

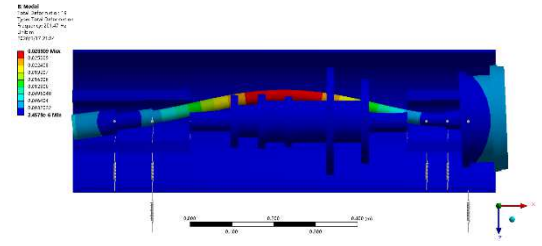
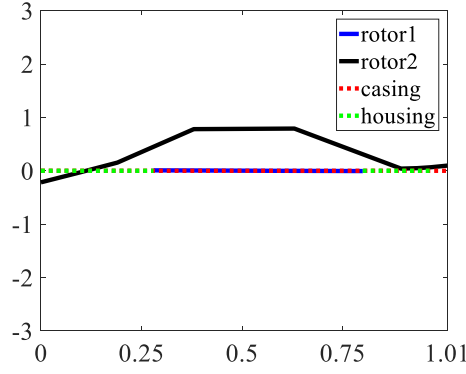


(a) 1st vibrational mode



(b) 2nd vibrational mode





(c) 3rd vibrational mode

Fig. 7 Comparison of the first three modes between the proposed model (left) and 3D model (right)

4 Results and discussions

4.1. Dynamic response of the whole engine without rubbing

The nonlinear response of the whole machine without rubbing is studied in this Section. SFDs are installed on No.2, No.3, No.4 and No.6 bearings. The initial elastic supporting stiffness is $2.5 \times 10^7 \text{ N/m}$. No. 1 and No. 5 bearings are set as rigid supports with initial stiffnesses equal to $10 \times 10^7 \text{ N/m}$. The rotating speed ratio is 1.5. The unbalance on node5 is $1 \times 10^{-5} \text{ kg}\cdot\text{m}$ and on node14 is $2 \times 10^{-5} \text{ kg}\cdot\text{m}$.

4.1.1 VC vibration of rolling bearing

When the rolling body passes through the loading zone periodically, it will cause varying stiffness excitation. When the frequency of the parametric excitation is close to the natural frequencies of the rotor system under certain parameter conditions and load conditions, it may cause resonance, which is regarded as VC vibration. The VC vibrational frequency is B_n times the rotating frequency. B_n is a number related to the radius of the inner and outer ring and the number of rolling bodies, which can be expressed by,

$$B_n = \frac{R_i}{R_o + R_i} \times N_b \quad (30)$$

Table 4 Parameters of bearing and SFD

Parameter	No.1	No.2	No.3	No.4	No.5	No.6
R_0 (m)	0.05	0.0375	0.0375	0.0375	0.0375	0.0375
R_i (m)	0.03	0.0225	0.025	0.025	0.0225	0.0225
N_b	18	18	18	18	18	18
γ_0 (m)	1×10^{-6}					
C_b	1.5×10^{10}					
	$\text{N/m}^{3/2}$	$\text{N/m}^{10/9}$	$\text{N/m}^{3/2}$	$\text{N/m}^{10/9}$	$\text{N/m}^{3/2}$	$\text{N/m}^{3/2}$
B_n	6.75	6.75	7.2	7.2	6.75	6.75
R (m)		0.04	0.04	0.04		0.04
L (m)		0.015	0.015	0.015		0.015
C (m)		2×10^{-4}	2×10^{-4}	2×10^{-4}		2×10^{-4}
μ (Pa·s)		3.8×10^{-3}	3.8×10^{-3}	3.8×10^{-3}		3.8×10^{-3}

B_{n1} and B_{n2} have values equal to the VC frequency multiplied by the rotating frequency for rotor1 and rotor2, respectively. f_{vc1} and f_{vc2} are the VC frequencies of rotor1 and rotor2 respectively. According to the bearing parameters, B_{n1} is 7.2 for rotor1 and B_{n2} is 6.75 for rotor2 as shown in Table 4. VC frequency at low rotating speed is shown in Fig. 8 and Fig. 9 for rotor1 and rotor2,

respectively. In this case, the VC frequency and its octave are easy to be observed. Fukata et al. [55] found that the rotating frequency of the ball and its harmonic are the main frequency component when the rotating speed is far away from the critical speed, which is consistent with the results in this paper.

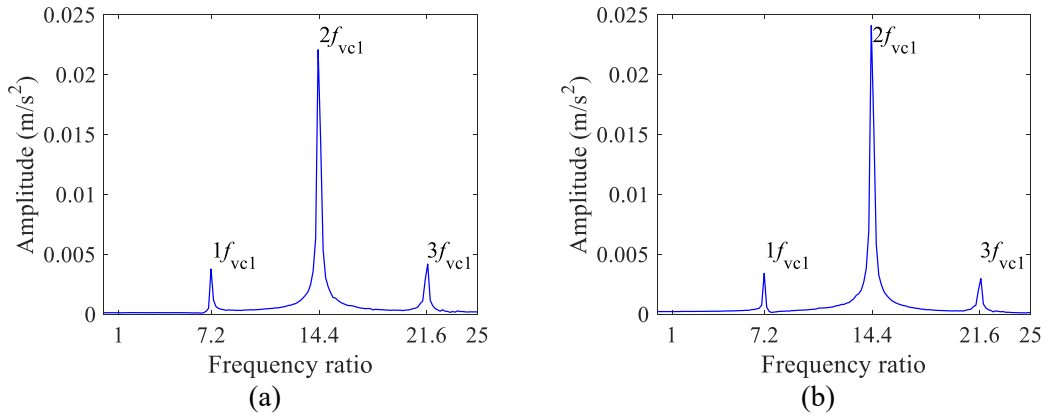


Fig. 8 Frequency response in the y-direction of (a) node 1 and (b) node 7 ($\omega_1=900\text{rpm}/15\text{Hz}$, $\omega_2=600\text{rpm}/10\text{Hz}$)

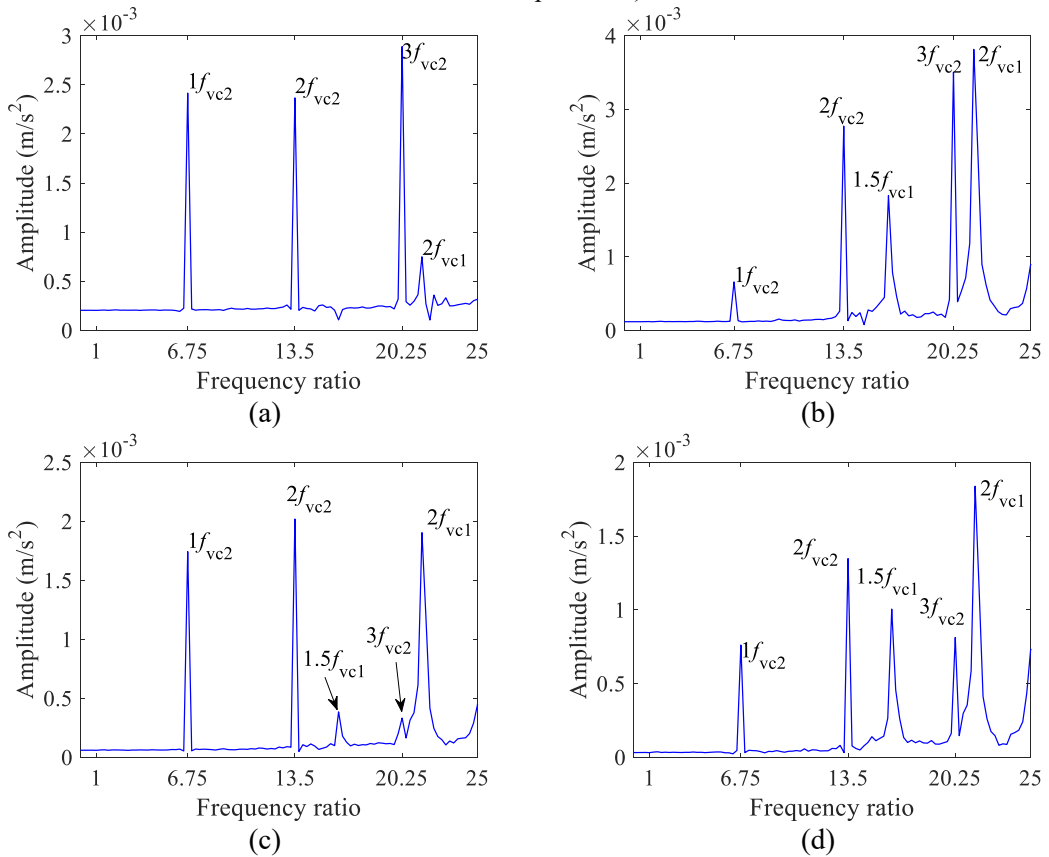


Fig. 9 Frequency response in the y-direction of (a) node 9, (b) node 10, (c) node 13, (d) node 15 ($\omega_1=900\text{rpm}/15\text{Hz}$, $\omega_2=600\text{rpm}/10\text{Hz}$)

4.1.2 Effect of the rotating speed on bifurcation

Keeping the unbalances unchanged, the effect of rotating speed on bifurcation characteristics is studied with parameters in Table 4 in this Section. Node 5 and 14 are selected as observation points for rotor1 and rotor2, respectively. Two sets of support stiffness are adopted as shown in Table 5. The rotating speed of rotor1 and rotor2 vary in [6300-42300] rpm and [4200-28200] rpm respectively. Bifurcation diagrams of rotor1 and rotor2 are shown in Fig. 10 and Fig. 11, respectively.

Table 5 Support stiffness at six supports ($\times 10^7 \text{N/m}$)

	No.1	No.2	No.3	No.4	No.5	No.6
Group1	10	2.5	2.5	2.5	10	2.5
Group2	5	1.5	1.5	1.0	5	1.5

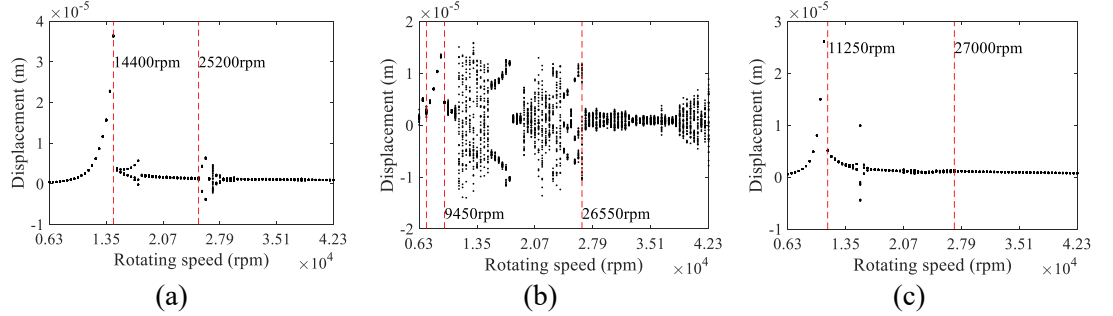


Fig. 10 Bifurcation diagram of rotor1 (a) with support stiffness in Group1, $\gamma_0=1\mu\text{m}$ (b) with support stiffness in Group1, $\gamma_0=10\mu\text{m}$ (c) with support stiffness in Group2, $\gamma_0=1\mu\text{m}$

As shown in Fig. 10 (a), with higher support stiffness and smaller bearing clearance, the dynamic response of rotor1 varies with the rotating speed as follows. When $\omega_1 < 14400$ rpm, rotor1 is in the motion of period 1; When $14400 \text{ rpm} < \omega_1 < 25200$ rpm, period-doubling appears, with the increase of rotating speed, the system motion is quasi-periodic; When $\omega_1 > 25200$ rpm, through inverse bifurcation, rotor1 gets out of quasi-periodic and returns to the motion of period 1.

When the bearing clearance increases under the same supporting stiffness as used in Fig. 10 (a), the bifurcation of rotor1 is shown in Fig. 10 (b), the nonlinear components of the system become more apparent. When $\omega_1 < 7200$ rpm, VC vibration becomes more obvious as the clearance of rolling bearing increases, the motion is quasiperiodic. When $7200 \text{ rpm} < \omega_1 < 9450$ rpm, with the increase of ω_1 , the rotating frequency gradually becomes the main component, the motion is periodic. When $9450 \text{ rpm} < \omega_1 < 26550$ rpm, the motion of rotor1 enters chaos through period-doubling bifurcation and then gets out of chaos by an explosive bifurcation. When $\omega_1 > 26550$ rpm, the motion is quasiperiodic. It can be seen that a larger bearing clearance will bring serious nonlinearity and strongly increases the instability of the system.

Fig. 10 (c) represents the bifurcation at a lower support stiffness in comparison with Fig. 10 (a). Rotor1 takes a series of motions as $\{P1 \rightarrow P3 \rightarrow P1\}$. Compared with Fig. 10 (a), the motion form of period 1 occupies a longer rotating speed range which indicates that the lower support stiffness will result in better stability.

As shown in Fig. 11 (a), with higher support stiffness and smaller bearing clearance, the dynamic response of rotor2 varies with the rotating speed as follows: When $\omega_2 < 15000$ rpm, the rotor2 enters quasiperiodic through period-doubling bifurcation. With the increase of ω_2 , the motion is periodic until 27300 rpm. When $\omega_2 > 27300$ rpm, quasiperiodic appears through period-doubling.

When the bearing clearance increases under the same supporting stiffness as in Fig. 11 (a), the bifurcation of rotor2 is shown in Fig. 11 (b), the nonlinear components of the system become more apparent. The motion of Rotor2 enters chaos through an explosive bifurcation when $\omega_2 < 7200$ rpm. Then, the motion is mainly in chaos. It can be seen that a larger bearing clearance will bring serious nonlinearity and make the motion form of the system very unstable.

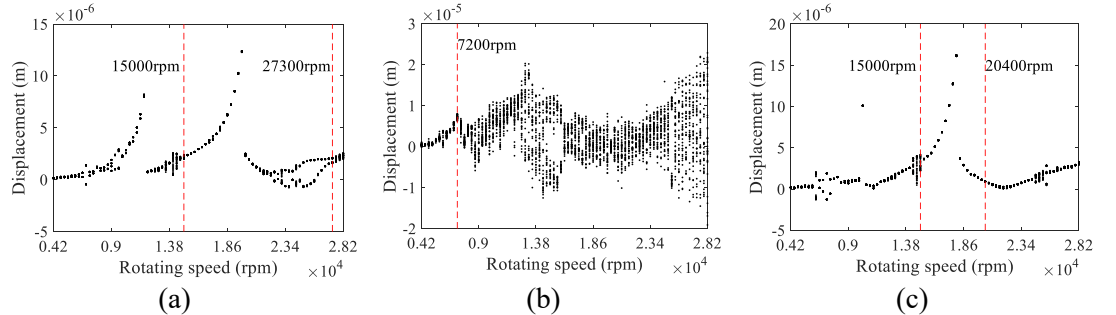


Fig. 11 Bifurcation diagram of rotor2 (a) with support stiffness in Group1, $\gamma_0=1\mu\text{m}$ (b) with support stiffness in Group1, $\gamma_0=10\mu\text{m}$ (c) with support stiffness in Group2, $\gamma_0=1\mu\text{m}$

Fig. 11 (c) represents the bifurcation at a lower support stiffness in comparison with Fig. 11 (a). When $\omega_2 < 15000$ rpm, the rotor2 enters quasiperiodic through period-doubling bifurcation. When $15000 \text{ rpm} < \omega_2 < 20400$ rpm, the motion is period1. When $\omega_2 > 20400$ rpm, period-doubling

appears, with the increase of rotating speed, the system gets into quasiperiodic finally. Compared with Fig. 11 (a), the motion form of period 1 occupies a longer rotating speed range which indicates that the lower support stiffness can make better stability.

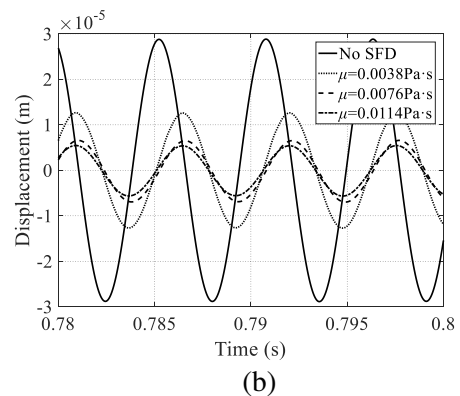
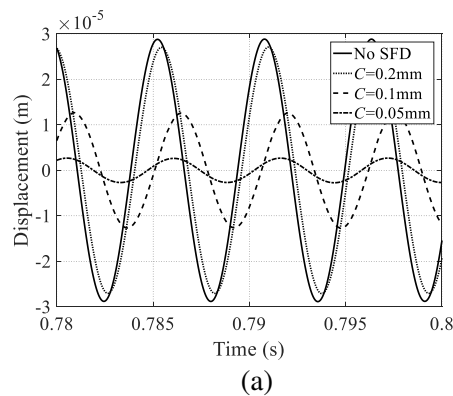
4.1.3 Damping effect of the SFD

The function of the SFD is to reduce vibration. The design of the SFD should be conducted to achieve a favorable damping effect in the design stage of the whole machine structure. It can be seen from Equation (6) that the main parameters affecting the oil film force are the clearance of SFD C , the viscosity of lubricating oil μ , damper length L and damper radius R . By keeping the structural parameters and bearing parameters unchanged, the influence of SFD parameters on the damping effect is studied in this Section. The steady response of node 4 on rotor1 and node 14 on rotor2 are selected to observe the effect of vibration reduction.

As shown in Fig. 10 (a) and Fig. 11 (a), the first critical speed of rotor1 is 10800rpm, the first critical speed of rotor2 is 10200rpm. Steady responses of rotor1 and rotor2 at critical speeds are shown in Fig. 12 and Fig. 13, respectively. The vibration reduction efficiency of rotor1 and rotor2 are shown in Table 6 and Table 7, respectively. The initial parameters of SFD are set as $\mu=3.8\times 10^{-3}$ Pa·s, $L=15$ mm and $R=40$ mm. The steady responses of rotor1 and rotor2 with different C are shown in Fig. 12 (a) and Fig. 13 (a), respectively. Because C is inversely proportional to the oil film force, with the decrease of C , the vibration reduction effect becomes more remarkable. When the thickness of the oil film is less than 0.1mm, the vibration amplitude is greatly reduced. When $C=0.05$ mm, the vibration reduction efficiency of rotor1 is 90.7%, and the vibration reduction efficiency of rotor2 is 87.1%. However, the decrease of oil film thickness will increase the difficulty of processing and manufacturing. Therefore, $C=0.1$ mm is chosen in the following study. The influence of lubricating oil viscosity on the damping effect is further studied which are shown in Fig. 12 (b) and Fig. 13 (b). As it can be seen, a higher viscosity will increase the damping effect. When $\mu=1.14\times 10^{-2}$ Pa·s, the vibration reduction efficiency of rotor1 is 81.2%, and the vibration reduction efficiency of rotor2 is 69.8%. Compared with mechanical manufacturing, an optimized lubricating oil viscosity is not difficult to achieve. Therefore, $\mu=1.14\times 10^{-2}$ Pa·s is chosen, the influence of different oil film lengths on vibration reduction is further studied in Fig. 12 (c) and Fig. 13 (c). The oil film length L is a key parameter for the oil film force. Numerical results show that a larger oil film length can achieve a better damping effect. When $L=20$ mm, the vibration reduction efficiency of rotor1 is 89.8%, and the vibration reduction efficiency of rotor2 is 86.1%. Therefore, $L=20$ mm is chosen, the influence of different oil film radius on vibration reduction is further studied in Fig. 12 (d) and Fig. 13 (d). It is noted that the effect of oil film radius on vibration reduction is not significant after the design of the previous three parameters. Finally, with the optimized SFD parameters which are $C=0.1$ mm, $\mu=1.14\times 10^{-2}$ Pa·s, $L=20$ mm, $R=50$ mm, the final vibration reduction efficiency of rotor1 is 91.4%, and the final vibration reduction efficiency of rotor2 is 87.3%, respectively.

Table 6 Vibration reduction efficiency of rotor1

C (mm)	Efficiency	μ (Pa·s)	Efficiency	L (mm)	Efficiency	R (mm)	Efficiency
0.2	5.9%	0.0038	56.2%	10	49.7%	40	89.8%
0.1	56.1%	0.0076	77.3%	15	81.2%	45	90.7%
0.05	90.7%	0.0114	81.2%	20	89.8%	50	91.4%



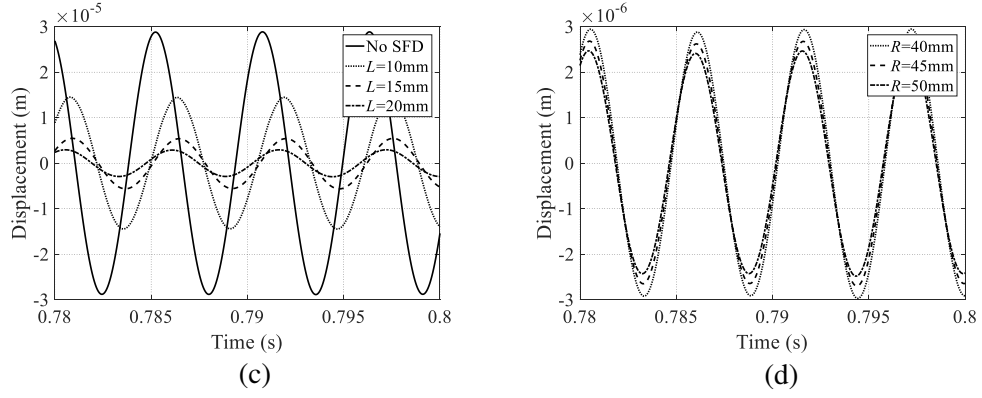


Fig. 12 Steady response of node 5 on 10800 rpm

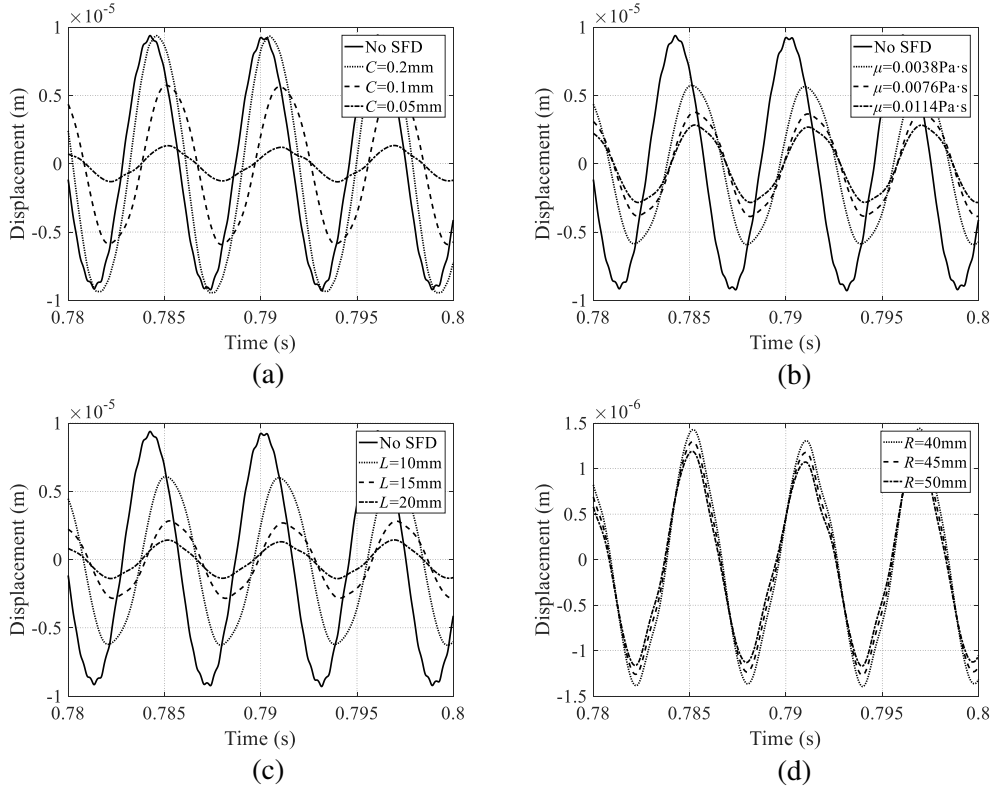


Fig. 13 Steady response of node 14 on 10200 rpm

Table 7 Vibration reduction efficiency of rotor2

C (mm)	Efficiency	μ (Pa·s)	Efficiency	L (mm)	Efficiency	R (mm)	Efficiency
0.2	0.06%	0.0038	39.9%	10	35.2%	40	84.8%
0.1	38.8%	0.0076	61.2%	15	71.4%	45	86.2%
0.05	87.1%	0.0114	69.8%	20	86.1%	50	87.3%

4.2 Dynamic response of the whole engine with rubbing

To study the nonlinear effect and evolution mechanism of single point blade-casing rubbing on the whole engine system, the nonlinear dynamic responses under linear and nonlinear supporting conditions are studied respectively in this Section. The number of blades is $N=20$, the coefficient of friction is $f=0.3$, the initial clearance δ is 10^{-6} m. The deformation of the casing at $\theta=180^\circ$ is $A=5 \times 10^{-6}$ m, the deformation ranges in $\beta=5^\circ$. The unbalance on node5 is 1×10^{-5} kg·m and on node14 is 2×10^{-5} kg·m.

4.2.1 Bifurcation analysis with linear support

In this Section, the connection between the rotor and the housing is simplified as a linear spring without considering bearing and SFD, and the support stiffness in Group2 of Table 5 is adopted. The bearing clearance $\gamma_0=1\mu\text{m}$, the rotating speed ratio $\lambda=1.5$. Under the linearized supporting condition, the rubbing stiffness k_c is the main parameter to be considered. The bifurcation diagrams of rotor1 and rotor2 with the change of rotating speed are shown in Fig. 14 and Fig. 15.

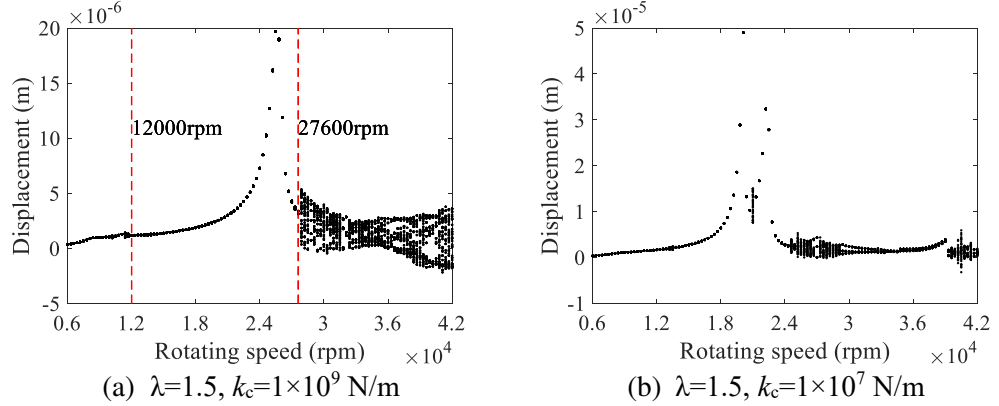


Fig. 14 Bifurcation diagram of rotor1

As shown in Fig. 14 (a), when $\omega_1 < 12000 \text{ rpm}$, the motion is quasi-periodic mainly because the rubbing frequency plays a major role when the rotating frequency is lower. When $12000 \text{ rpm} < \omega_1 < 27600 \text{ rpm}$, the motion is period 1. When $\omega_1 > 27600 \text{ rpm}$, rotor1 enters chaos through Neimark-Sacker bifurcation. Fig. 14 (b) is bifurcation diagrams with lower rubbing stiffness. By comparing the bifurcation diagram with higher rubbing stiffness, it can be found that the amplitude at the resonant peak significantly increases, and the resonance frequency shifts to the left. In the case of lower rubbing stiffness, more periodic motion and less chaotic motion occur. The lower rubbing stiffness can reduce the quasiperiodic and chaotic characteristics of rotor1.

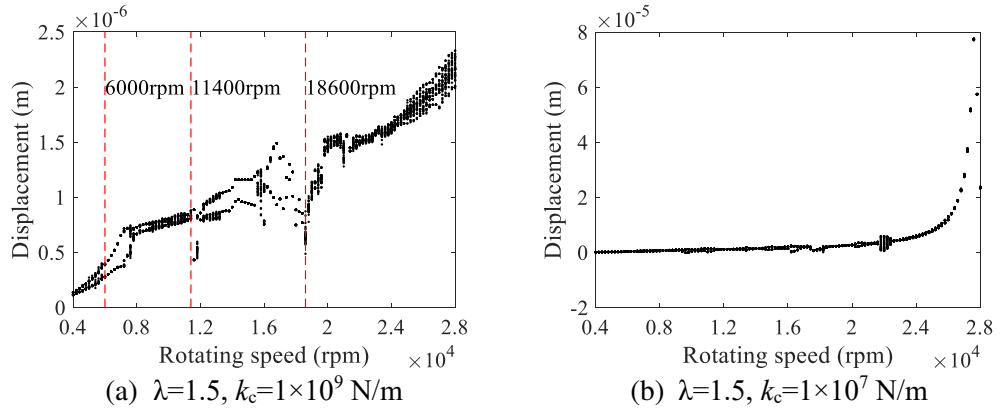


Fig. 15 Bifurcation diagram of rotor2

As shown in Fig. 15 (a), when $\omega_2 < 6000 \text{ rpm}$, the motion is periodic mainly because the rubbing frequency plays a major role when the rotating frequency is lower. When $6000 \text{ rpm} < \omega_2 < 11400 \text{ rpm}$, period-doubling appears, rotor2 enters quasiperiodic through period-doubling bifurcation. With ω_2 increasing, rotor2 gets out of quasiperiodic through inverse doubling bifurcation when $11400 \text{ rpm} < \omega_2 < 18600 \text{ rpm}$, and then periodic motion and chaotic motion appear alternately when $\omega_2 > 18600 \text{ rpm}$. Through explosive chaos, rotor2 finally enters the chaos motion.

Fig. 15 (b) is a bifurcation diagram with lower rubbing stiffness. By comparing the bifurcation diagram with higher rubbing stiffness, it can be found that the amplitude at the resonant peak significantly increases, and the resonance frequency shifts to the left. In the case of lower rubbing stiffness, more periodic motion occurs. Rotor2 with rigid and elastic supports is more stable than rotor1 with full elastic supports.

4.2.2 Bifurcation analysis with nonlinear support

In real aero-engines, the supporting conditions are nonlinear, and the nonlinear mechanism in rubbing fault cannot be correctly reflected based on the linearization hypothesis. In this Section, the rubbing of the blade casing under the nonlinear supporting conditions with the rolling bearing and the SFD in Table 4 are comprehensively considered. The rubbing stiffness $k_c=1\times 10^9 \text{ N/m}$. The

rotating speed ratio λ and bearing clearance γ_0 are the two parameters to be considered. The bifurcation diagrams of rotor1 and rotor2 with the change of rotating speed are shown in Fig. 16 and Fig. 17, respectively.

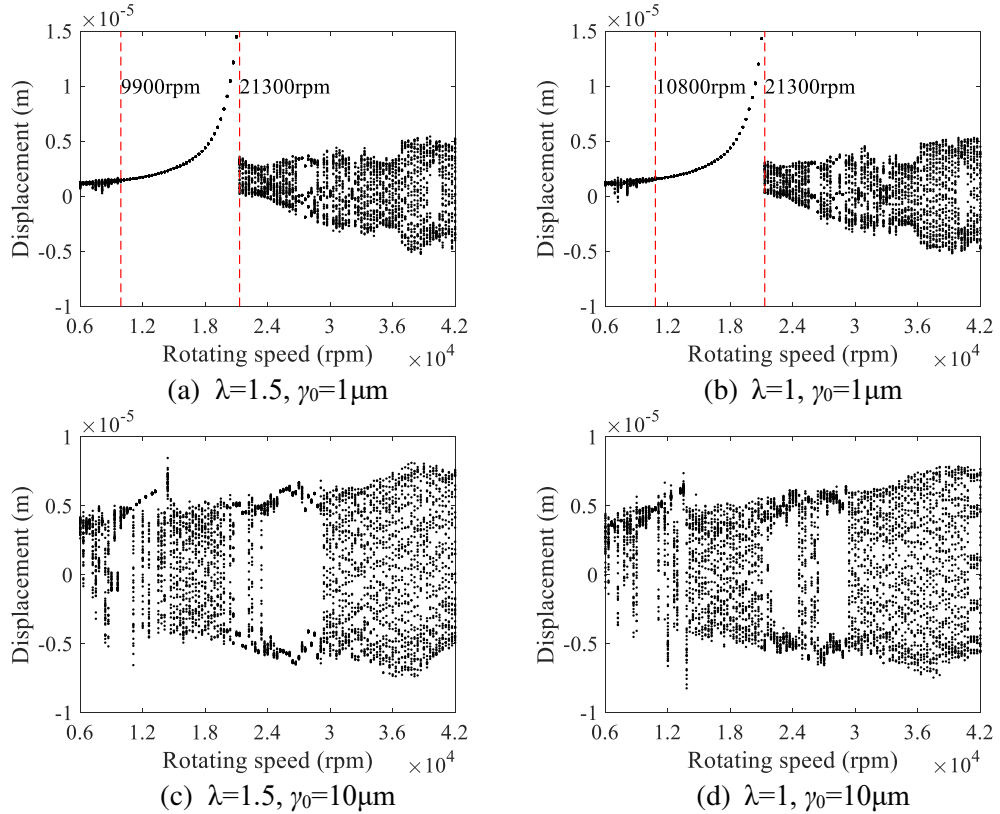


Fig. 16 Bifurcation diagram of rotor1 with nonlinear support

As shown in Fig. 16 (a), when $\omega_1 < 9900$ rpm, the motion of rotor1 is quasi-periodic mainly because VC frequency plays a major role when the rotating frequency is lower. When $9900 \text{ rpm} < \omega_1 < 21000$ rpm, the VC vibration is weak, the motion is period 1. When $\omega_1 > 21000$ rpm, rotor1 enters quasiperiodic through Neimark-Sacker bifurcation. Rotor1 gets into chaos finally through explosive chaos. It can be seen in Fig. 16 (b), when the rotating speed ratio is 1, the motion of rotor1 does not change much, except that the quasi-periodic interval caused by VC vibration extends to 10800rpm.

By comparing the bifurcation diagram without rubbing in Fig. 10 (c), it can be found from Fig. 16 (a) that rubbing force significantly reduces the amplitude at the resonant peak, and the resonance frequency shifts to the right, which indicates that rubbing introduces the characteristics of a hard spring.

Compared with the linear support case in Fig. 14 (a), the nonlinear support case in Fig. 16 (a) has the following changes: (1) The response at the resonant peak decrease; (2) The quasi-periodic motion is more obvious in the low-speed region; (3) Chaos occurs earlier in the high-speed region.

Fig. 16 (c) and Fig. 16 (d) are bifurcation diagrams with higher bearing clearance at the above two rotating speed ratios, respectively. It can be found that significant quasi-periodic and chaotic motions occur, which indicates that higher bearing clearance will increase the instability of the system under rubbing fault. The influence of the rotating speed ratio is not obvious.

As shown in Fig. 17 (a) and Fig. 17 (b), when $\omega_2 < 24600$ rpm, the motion of rotor2 is periodic and quasi-periodic. When $\omega_2 > 24600$ rpm, the motion of rotor2 enters period 1. When $\omega_2 > 27900$ rpm in Fig. 17 (b), the motion is mainly quasi-periodic. As shown in Fig. 17 (c) and Fig. 17 (d), when the bearing clearance is higher, the motion of the system becomes more unstable, and the motion is mainly periodic and chaotic.

By comparing the bifurcation diagram without rubbing in Fig. 11(c), it can be found from Fig. 17 (a) that the resonance frequency shifts to the right, rubbing force increases the amplitude at the resonant peak which presents different characteristics with rotor1. This phenomenon indicates that under all elastic support conditions, the rubbing force will increase the additional stiffness, while under the conditions of rigid support and elastic support, the influence of the rubbing force on the additional stiffness is not obvious.

Compared with the linear support case in Fig. 15 (a) and the nonlinear support case as shown in Fig. 17 (a), the motions of rotor2 show similar characteristics which are mainly periodic and

quasi-periodic in the low rotating speed region. However, in the high rotating speed region, the motion in Fig. 17 (a) is more stable than that in Fig. 15 (a).

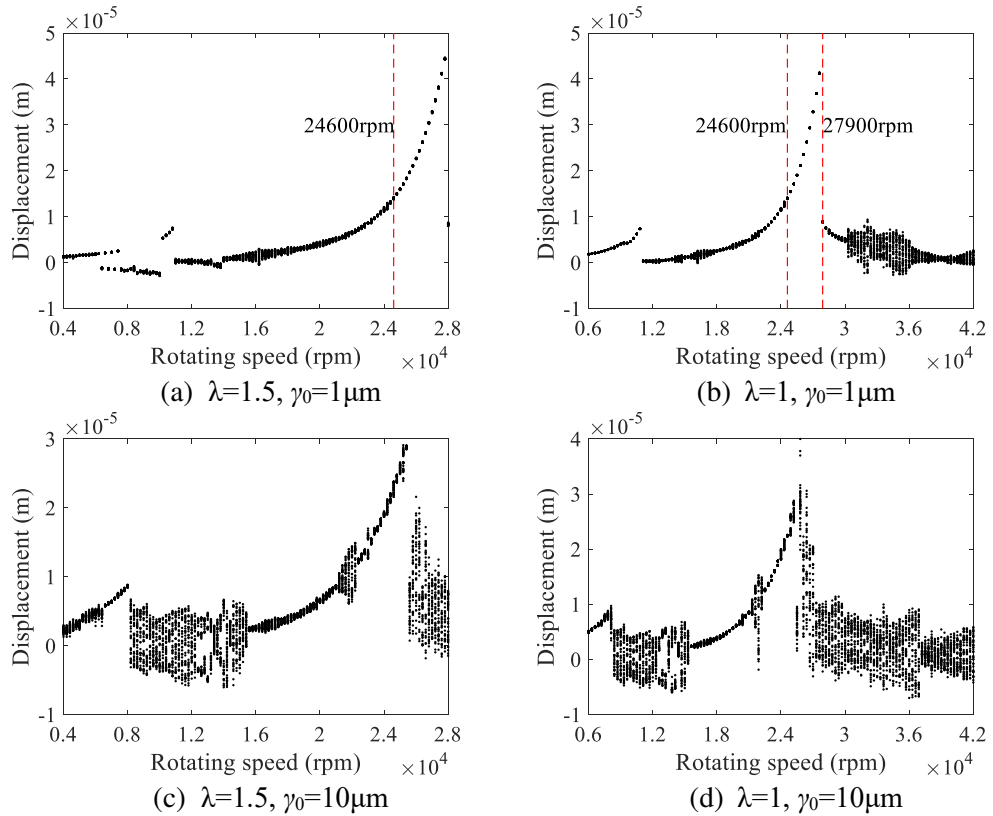


Fig. 17 Bifurcation diagram of rotor2 with nonlinear support

5 Conclusions

A dual-rotor whole aeroengine model with rolling bearing and SFD is established. The accuracy of the linear part of the model is first verified by its corresponding 3D finite element model formulated. The effectiveness of the nonlinear support is verified by the VC vibration frequency and the damping effect of the SFD. The nonlinear dynamic behavior of the whole aeroengine with rubbing fault under the nonlinear support is detailedly investigated. The following conclusions can be drawn:

(1) VC vibration is easy to occur in the low rotating speed region, especially in the case with larger bearing clearance and rubbing fault and has a significant impact on the stability of the system.

(2) It can be seen from the bifurcation analysis that when rubbing is not occur in the whole aeroengine, a more stable system motion form can be obtained by using lower bearing stiffness and lower bearing clearance.

(3) A small oil film thickness can provide a very good effect on vibration reduction, but the design of SFDs can focus on the lubricating oil viscosity and oil film length after the oil film thickness has been determined to satisfy the convenience of processing and manufacturing. Oil film radius has a relatively weak impact on the vibration reduction, it can be selected as the bearing outer diameter or the bearing housing inner diameter in the simulation model.

(4) The motion of period, quasiperiodic and chaos are observed in the case of rubbing fault with both linear supports and nonlinear supports. Period-doubling bifurcation and explosive bifurcation are the routes to chaos.

(5) The rubbing fault in the nonlinear support case will excite more significant VC vibration in the low-speed region and expand the rotating speed range of the chaotic region in the high-speed region compared with that in the linear support case.

(6) When the rubbing fault occurs, the speed ratio has little influence on the stability of the system. However, a smaller rubbing stiffness and a smaller bearing clearance will be beneficial to achieve better system stability.

Acknowledgments

The research work is supported by the National Science and Technology Major Project (2017-I-0006-0007), the National Natural Science Foundation of China (11572086, 52005100), the Jiangsu Natural Science Foundation (BK20170022, BK20180062, BK20190324), the Fundamental Research Funds for the Central Universities (2242020k1G010), the Six Talents Peaks Project in Jiangsu Province (KTHY-005).

Compliance with ethical standards

Conflict of interest The authors declare that they have no conflict of interest.

References

- [1]. Prabith, K., Krishna, I.R.P.: The numerical modeling of rotor–stator rubbing in rotating machinery: a comprehensive review. *Nonlinear Dyn.* 101, 1317–1363 (2020). <https://doi.org/10.1007/s11071-020-05832-y>
- [2]. Hong, J., Chen, M., and Liu, S.: Application of whole engine finite element models in aero-engine rotordynamic simulation analysis, ASME Turbo Expo 2007: Power for Land, Sea, and Air. American Society of Mechanical Engineers, ASME, 771–778 (2007).
- [3]. Zuo, Y., Wang, J.: A method for dynamic analysis of three-dimensional solid element rotors with uncertain parameters. *J. Eng. Gas Turbines Power.* 139, (2017). <https://doi.org/10.1115/1.4035049>
- [4]. Qu, M.J., Chen, G.: Effect of the aero-engine mounting stiffness on the whole engine coupling vibration. *J. Eng. Gas Turbines Power.* 140, (2018). <https://doi.org/10.1115/1.4038542>
- [5]. Ma, Y., Zhao, Q., Zhang, K., Xu, M., Zhao, W.: Analysis of Instantaneous Vibrational Energy Flow for an Aero-Engine Dual-Rotor–Support–Casing Coupling System. *J. Eng. Gas Turbines Power.* 142, (2020). <https://doi.org/10.1115/1.4046418>
- [6]. Sinou, J.J.: Non-linear dynamics and contacts of an unbalanced flexible rotor supported on ball bearings. *Mech. Mach. Theory.* 44, 1713–1732 (2009). <https://doi.org/10.1016/j.mechmachtheory.2009.02.004>
- [7]. Bai, C., Zhang, H., Xu, Q.: Subharmonic resonance of a symmetric ball bearing-rotor system. *Int. J. Non. Linear. Mech.* 50, 1–10 (2013). <https://doi.org/10.1016/j.ijnonlinmec.2012.11.002>
- [8]. Lu, Z., Wang, X., Hou, L., Chen, Y., Liu, X.: Nonlinear response analysis for an aero engine dual-rotor system coupled by the inter-shaft bearing. *Arch. Appl. Mech.* 89, 1275–1288 (2019). <https://doi.org/10.1007/s00419-018-01501-0>
- [9]. Yang, Y., Liu, C., Jiang, D., Behdinan, K.: Nonlinear vibration signatures for localized fault of rolling element bearing in rotor-bearing-casing system. *Int. J. Mech. Sci.* 173, (2020). <https://doi.org/10.1016/j.ijmecsci.2020.105449>
- [10]. Lu, Z., Zhong, S., Chen, H., Wang, X., Han, J., Wang, C.: Nonlinear response analysis for a dual-rotor system supported by ball bearing. *Int. J. Non. Linear. Mech.* 128, 103627 (2021). <https://doi.org/10.1016/j.ijnonlinmec.2020.103627>
- [11]. Lu, K., Jin, Y., Huang, P., Zhang, F., Zhang, H., Fu, C., Chen, Y.: The applications of POD method in dual rotor-bearing systems with coupling misalignment. *Mech. Syst. Signal Process.* 150, 107236 (2021). <https://doi.org/10.1016/j.ymsp.2020.107236>
- [12]. Defaye, C., Nelias, D., Leblanc, A., Bon, F.: Theoretical analysis of high-speed cylindrical roller bearing with flexible rings mounted in a squeeze film damper. *Tribol. Trans.* 51, 762–770 (2008). <https://doi.org/10.1080/10402000801911804>
- [13]. Schweizer, B.: Oil whirl, oil whip and whirl/whip synchronization occurring in rotor systems with full-floating ring bearings. *Nonlinear Dyn.* 57, 509–532 (2009). <https://doi.org/10.1007/s11071-009-9466-3>
- [14]. Inayat-Hussain, J.I.: Bifurcations in the response of a flexible rotor in squeeze-film dampers with retainer springs. *Chaos, Solitons and Fractals.* 39, 519–532 (2009). <https://doi.org/10.1016/j.chaos.2007.01.086>
- [15]. Boyaci, A., Lu, D., Schweizer, B.: Stability and bifurcation phenomena of Laval/Jeffcott rotors in semi-floating ring bearings. *Nonlinear Dyn.* 79, 1535–1561 (2015). <https://doi.org/10.1007/s11071-014-1759-5>
- [16]. Woschke, E., Daniel, C., Nitzschke, S.: Excitation mechanisms of non-linear rotor systems with floating ring bearings - simulation and validation. *Int. J. Mech. Sci.* 134, 15–27 (2017). <https://doi.org/10.1016/j.ijmecsci.2017.09.038>
- [17]. Chen, H., Hou, L., Chen, Y., Yang, R.: Dynamic characteristics of flexible rotor with squeeze

- film damper excited by two frequencies. *Nonlinear Dyn.* 87, 2463–2481 (2017). <https://doi.org/10.1007/s11071-016-3204-4>
- [18]. Hamzehlouia, S., Behdinin, K.: Squeeze film dampers supporting high-speed rotors: Rotordynamics. *Proc. Inst. Mech. Eng. Part J J. Eng. Tribol.* 235, 495–508 (2021). <https://doi.org/10.1177/1350650120922082>
- [19]. Chen, X., Gan, X., Ren, G.: Nonlinear responses and bifurcations of a rotor-bearing system supported by squeeze-film damper with retainer spring subjected to base excitations. Springer Netherlands (2020)
- [20]. Zhou, H. lun, Luo, G. huo, Chen, G., Wang, F.: Analysis of the nonlinear dynamic response of a rotor supported on ball bearings with floating-ring squeeze film dampers. *Mech. Mach. Theory.* 59, 65–77 (2013). <https://doi.org/10.1016/j.mechmachtheory.2012.09.002>
- [21]. Zhang, J., Lu, X., Lin, J., Ma, L., Wang, J.: Dynamic Analysis of a Rotor-Bearing-SFD System with the Bearing Inner Race Defect. *Shock Vib.* 2017, (2017). <https://doi.org/10.1155/2017/2489376>
- [22]. Luo, Z., Wang, J., Tang, R., Wang, D.: Research on vibration performance of the nonlinear combined support-flexible rotor system. *Nonlinear Dyn.* 98, 113–128 (2019). <https://doi.org/10.1007/s11071-019-05176-2>
- [23]. Ma, X., Ma, H., Qin, H., Guo, X., Zhao, C., Yu, M.: Nonlinear vibration response characteristics of a dual-rotor-bearing system with squeeze film damper. *Chinese J. Aeronaut.* (2021). <https://doi.org/10.1016/j.cja.2021.01.013>
- [24]. Chen, G.: A new rotor-ball bearing-stator coupling dynamics model for whole aero-engine vibration. *J. Vib. Acoust. Trans. ASME.* 131, 0610091–0610099 (2009). <https://doi.org/10.1115/1.4000475>
- [25]. Chen, G.: Vibration modelling and verifications for whole aero-engine. *J. Sound Vib.* 349, 163–176 (2015). <https://doi.org/10.1016/j.jsv.2015.03.029>
- [26]. Hai, P.M., Bonello, P.: An impulsive receptance technique for the time domain computation of the vibration of a whole aero-engine model with nonlinear bearings. *J. Sound Vib.* 318, 592–605 (2008). <https://doi.org/10.1016/j.jsv.2008.04.033>
- [27]. Bonello, P., Minh Hai, P.: A receptance harmonic balance technique for the computation of the vibration of a whole aero-engine model with nonlinear bearings. *J. Sound Vib.* 324, 221–242 (2009). <https://doi.org/10.1016/j.jsv.2009.01.039>
- [28]. Bonello, P., Hai, P.M.: Computational studies of the unbalance response of a whole aero-engine model with squeeze-film bearings. *J. Eng. Gas Turbines Power.* 132, 1–7 (2010). <https://doi.org/10.1115/1.3159381>
- [29]. Groves, K.H., Bonello, P., Hai, P.M.: Efficient dynamic analysis of a whole aeroengine using identified nonlinear bearing models. *Proc. Inst. Mech. Eng. Part C J. Mech. Eng. Sci.* 226, 66–81 (2012). <https://doi.org/10.1177/0954406211412319>
- [30]. Bonello, P., Pham, H.M.: A theoretical and experimental investigation of the dynamic response of a squeeze-film damped twin-shaft test rig. *Proc. Inst. Mech. Eng. Part C J. Mech. Eng. Sci.* 228, 218–229 (2014). <https://doi.org/10.1177/0954406213484223>
- [31]. Ma, H., Yin, F., Guo, Y., Tai, X., Wen, B.: A review on dynamic characteristics of blade–casing rubbing. *Nonlinear Dyn.* 84, 437–472 (2016). <https://doi.org/10.1007/s11071-015-2535-x>
- [32]. Gustavsson, R.K., Aidanpää, J.O.: Evaluation of impact dynamics and contact forces in a hydropower rotor due to variations in damping and lateral fluid forces. *Int. J. Mech. Sci.* 51, 653–661 (2009). <https://doi.org/10.1016/j.ijmecsci.2009.07.002>
- [33]. Torkhani, M., May, L., Voinis, P.: Light, medium and heavy partial rubs during speed transients of rotating machines: Numerical simulation and experimental observation. *Mech. Syst. Signal Process.* 29, 45–66 (2012). <https://doi.org/10.1016/j.ymsp.2012.01.019>
- [34]. Ma, H., Shi, C., Han, Q., Wen, B.: Fixed-point rubbing fault characteristic analysis of a rotor system based on contact theory. *Mech. Syst. Signal Process.* 38, 137–153 (2013). <https://doi.org/10.1016/j.ymsp.2012.10.009>
- [35]. Ma, H., Lu, Y., Wu, Z., Tai, X., Wen, B.: Vibration response analysis of a rotational shaft-disk-blade system with blade-tip rubbing. *Int. J. Mech. Sci.* 107, 110–125 (2016). <https://doi.org/10.1016/j.ijmecsci.2015.12.026>
- [36]. Thiery, F., Gustavsson, R., Aidanpää, J.O.: Dynamics of a misaligned Kaplan turbine with blade-to-stator contacts. *Int. J. Mech. Sci.* 99, 251–261 (2015). <https://doi.org/10.1016/j.ijmecsci.2015.05.023>
- [37]. Salles, L., Staples, B., Hoffmann, N., Schwingshackl, C.: Continuation techniques for analysis of whole aeroengine dynamics with imperfect bifurcations and isolated solutions. *Nonlinear Dyn.* 86, 1897–1911 (2016). <https://doi.org/10.1007/s11071-016-3003-y>
- [38]. Sun, C., Chen, Y., Hou, L.: Steady-state response characteristics of a dual-rotor system induced by rub-impact. *Nonlinear Dyn.* 86, 91–105 (2016). <https://doi.org/10.1007/s11071-016-2874->

- [39]. Yang, Y., Cao, D., Yu, T., Wang, D., Li, C.: Prediction of dynamic characteristics of a dual-rotor system with fixed point rubbing—Theoretical analysis and experimental study. *Int. J. Mech. Sci.* 115–116, 253–261 (2016). <https://doi.org/10.1016/j.ijmecsci.2016.07.002>
- [40]. Mokhtar, M.A., Kamalakar Darpe, A., Gupta, K.: Investigations on bending-torsional vibrations of rotor during rotor-stator rub using Lagrange multiplier method. *J. Sound Vib.* 401, 94–113 (2017). <https://doi.org/10.1016/j.jsv.2017.03.026>
- [41]. Wang, N., Liu, C., Jiang, D., Behdinan, K.: Casing vibration response prediction of dual-rotor-blade-casing system with blade-casing rubbing. *Mech. Syst. Signal Process.* 118, 61–77 (2019). <https://doi.org/10.1016/j.ymsp.2018.08.029>
- [42]. Yu, P., Chen, G., Li, L.: Modal analysis strategy and nonlinear dynamic characteristics of complicated aero-engine dual-rotor system with rub-impact. *Chinese J. Aeronaut.* 1–23 (2021). <https://doi.org/10.1016/j.cja.2020.10.031>
- [43]. Ding, Q.: Backward Whirl and Its Suppression of a Squeeze Film Damper Mounted Rotor/Casing System in Passage through Critical Speed with Rubs. *J. Vib. Control*, 10, 561–573 (2004). <https://doi.org/10.1177/1077546041125827>
- [44]. Chang-Jian, C.W., Chen, C.K.: Chaos and bifurcation of a flexible rub-impact rotor supported by oil film bearings with nonlinear suspension. *Mech. Mach. Theory.* 42, 312–333 (2007). <https://doi.org/10.1016/j.mechmachtheory.2006.03.007>
- [45]. Shen, X., Jia, J., Zhao, M.: Numerical analysis of a rub-impact rotor-bearing system with mass unbalance. *JVC/Journal Vib. Control.* 13, 1819–1834 (2007). <https://doi.org/10.1177/1077546307080029>
- [46]. Shen, X., Jia, J., Zhao, M.: Nonlinear analysis of a rub-impact rotor-bearing system with initial permanent rotor bow. *Arch. Appl. Mech.* 78, 225–240 (2008). <https://doi.org/10.1007/s00419-007-0155-8>
- [47]. Hu, A., Hou, L., Xiang, L.: Dynamic simulation and experimental study of an asymmetric double-disk rotor-bearing system with rub-impact and oil-film instability. *Nonlinear Dyn.* 84, 641–659 (2016). <https://doi.org/10.1007/s11071-015-2513-3>
- [48]. Xiang, L., Hu, A., Hou, L., Xiong, Y., Xing, J.: Nonlinear coupled dynamics of an asymmetric double-disc rotor-bearing system under rub-impact and oil-film forces. *Appl. Math. Model.* 40, 4505–4523 (2016). <https://doi.org/10.1016/j.apm.2015.11.028>
- [49]. Wang, N., Jiang, D., Behdinan, K.: Vibration response analysis of rubbing faults on a dual-rotor bearing system. *Arch. Appl. Mech.* 87, 1891–1907 (2017). <https://doi.org/10.1007/s00419-017-1299-9>
- [50]. Jin, Y., Liu, Z., Yang, Y., Li, F., Chen, Y.: Nonlinear vibrations of a dual-rotor-bearing-coupling misalignment system with blade-casing rubbing. *J. Sound Vib.* 497, 22–37 (2021). <https://doi.org/10.1016/j.jsv.2021.115948>
- [51]. Chen, G., Li, C.G., Wang, D.Y.: Nonlinear dynamic analysis and experiment verification of rotor-ball bearings-support-stator coupling system for aeroengine with rubbing coupling faults. *J. Eng. Gas Turbines Power.* 132, 1–9 (2010). <https://doi.org/10.1115/1.2940355>
- [52]. Chen, G.: Simulation of casing vibration resulting from blade-casing rubbing and its verifications. *J. Sound Vib.* 361, 190–209 (2016). <https://doi.org/10.1016/j.jsv.2015.09.041>
- [53]. Yang, Y., Ouyang, H., Yang, Y., Cao, D., Wang, K.: Vibration analysis of a dual-rotor-bearing-double casing system with pedestal looseness and multi-stage turbine blade-casing rub. *Mech. Syst. Signal Process.* 143, (2020). <https://doi.org/10.1016/j.ymsp.2020.106845>
- [54]. Ma, L., Wang, J., Zhang, G.: The dynamic characteristic of a faulted rotor system with multi-objective optimization designed SFD. *Appl. Sci.* 9, (2019). <https://doi.org/10.3390/app9173628>
- [55]. Fukata, S., Gad, E.H., Kondou, T., Ayabe, T., Tamura, H. “On the Radial Vibration of Ball Bearings: Computer Simulation.” *Bulletin of JSME*, 28, 899-904. (1985.) <https://doi.org/10.1299/jsme1958.28.899>
- [56]. Gupta, P.K.: Dynamics of Rolling-Element Bearings Part I: Cylindrical Roller Bearing Analysis Generalized Equations of Roller Motion Dynamics of Rolling-Element Bearings Part I: Cylindrical Roller Bearing Analysis. (1979)
- [57]. Editorial Board of Aero-engine Design Manual Aero-engine Design Manual (19thPart): Rotor Dynamics and Whole Machine Vibration, Aerospace Industry Press, Beijing, 227-249 (2000.)
- [58]. Chen, G.: Simulation of casing vibration resulting from blade-casing rubbing and its verifications. *J. Sound Vib.* 361, 190–209 (2016). <https://doi.org/10.1016/j.jsv.2015.09.041>
- [59]. Lankarani, H. M., and Nikraves, P. E.: A contact force model with hysteresis damping for impact analysis of multibody systems. *J. Mech Design*, 112(3), 369-376. (1990) <https://doi.org/10.1115/1.2912617>